This is a post-peer-review version of an article published in RSC advances.

The final authenticated version is available online at: http://dx.doi.org/10.1039/c6ra23717g

Published under a “All rights reserved” license.

Please do not adjust margins

RSC Advances

ARTICLE

Orientation symmetry breaking in self-assembled $Ce_{1-x}Gd_xO_{2-y}$ nanowires derived from chemical solutions

Received 00th January 20xx,
Accepted 00th January 20xx

DOI: 10.1039/x0xx00000x

www.rsc.org/

A. Queraltó,[a,†] M. de la Mata,[a,b] L. Martínez,[c] C. Magén,[d] M. Gibert,[e] J. Arbiol,[b,f] R. Hühne,[g] X. Obradors[a] and T. Puig[a]

Understanding the growth mechanisms of nanostructures obtained from chemical solutions, a high-throughput production methodology, is essential to correlate precisely the growth conditions to the nanostructures' morphology, dimensions and orientation. It is shown that self-organized (011)-oriented $Ce_{0.9}Gd_{0.1}O_{2-y}$ (CGO) nanowires having a single in-plane orientation are achieved when an anisotropic (011)-$LaAlO_3$ (LAO) substrate is chosen. STEM and AFM images of the epitaxial nanowires reveal the (001)CGO[0-11]||(011)LAO[100] growth orientation, with the enlargement occurring along the [0-11]CGO direction with (111) lateral facets. The chosen substrate allowed us to study a unique case where the resulting biaxial strain is isotropic, while the dissimilar lateral surface energies are the key factor to obtain an energetically imbalanced and non-degenerated nanowire configuration. Rapid Thermal Annealing (RTA) has allowed to sort out experimentally nucleation from coarsening and to analyze the kinetic phenomena of the nanowires. A thermodynamic driving force is shown to exist for a continuous elongation of the nanowires while the coarsening rates are found to be strongly temperature dependent and so kinetic effects are the key factors to control the size and density of the self-organized nanowire system. A remarkably fast nanowires' growth rate (14-40 nm min^{-1}) is observed which we associate with a high atomic mobility probably linked to a high concentration of oxygen vacancies, as detected by XPS. These nanowires are envisaged as model systems pushing forward the study of low energetic and highly oxygen deficient {111} lateral facets useful for catalysis, gas sensors and ionic conductivity applications.

1 Introduction

The production of nanostructures has been an extremely investigated topic in the past years due to the unique functional properties that can be obtained at the nanoscale, for applications in catalysis, magnetism, optics, electronics, superconductivity, etc.[1-6] Two different strategies are typically used to fabricate nanostructures. While top-down approaches such as lithography may be reaching their limits in size reduction and shape design at the nanoscale,[7] bottom-up strategies based on the spontaneous formation of nanostructures through self-assembling and self-organization processes are arising as a promising route to fabricate very small devices with a high production rate and homogeneity in shape and size.[8, 9] A big effort is being dedicated to understand the mechanisms governing the thermodynamic and kinetic aspects that lead to the formation of different types of equilibrium shapes. Most research has been done in the field of semiconductors.[10, 11] However, complex oxides such as $Ce_{1-x}Gd_xO_{2-y}$, $La_{0.7}Sr_{0.3}MnO_3$ or $BaZrO_3$ have recently attracted a great interest due to their singular functional properties, small dimensions and high-throughput achieved.[10-15] The remarkable catalytic activity and oxygen ionic diffusivity of doped CeO_2 (e.g. $Ce_{1-x}Zr_xO_{2-y}$ and $Ce_{1-x}Gd_xO_{2-y}$)[16] is ideal for their use in applications such as oxygen gas sensing,[17-20] three way emission control catalysts (TWC),[21, 22] fuel cells and harvesting devices,[23-26] and as supports in heterogeneous catalysts.[27-29] Doped CeO_2 has also been studied for its use in electro-optical coatings due to their good optical properties in the visible/near infrared and ultraviolet regions,[30-32] but also as a replacement of silicon dioxide in electronic devices due to its high dielectric constant and compatibility with silicon[33, 34] or as buffer layer in high-temperature superconducting coating conductors.[35-37]

Chemical solution deposition (CSD) is an adaptable, low-cost and scalable methodology used to synthesize a wide range of functional oxide thin films and nanostructures with a precise control over stoichiometry, nucleation and growth.[14, 15, 38, 39] Conventional thermal annealing (CTA) by means of tubular

[a] Institut de Ciència de Materials de Barcelona (ICMAB-CSIC), Campus UAB, 08193 Bellaterra, Catalonia, Spain.
[b] Institut Català de Nanociència i Nanotecnologia (ICN2), CSIC and The Barcelona Institute of Science and Technology (BIST), Campus UAB, 08193 Bellaterra, Catalonia, Spain.
[c] Instituto de Ciencia de Materiales de Madrid (ICMM-CSIC), 28029 Cantoblanco, Madrid, Spain.
[d] Laboratorio de Microscopías Avanzadas (LMA), Instituto de Nanociencia de Aragón (INA) - ARAID and Departamento de Física de la Materia Condensada, Universidad de Zaragoza, 50018 Zaragoza, Aragón, Spain.
[e] Département de Physique de la Matière Quantique, University of Geneva, 24 Quai Ernest-Ansermet, 1211 Genève 4, Switzerland.
[f] Institució Catalana de Recerca i Estudis Avançats (ICREA), Pg. Lluís Companys 23, 08010 Barcelona, Catalonia, Spain.
[g] Institute for Metallic Materials, IFW Dresden, P.O. Box 270116, 01171 Dresden, Germany.
† Corresponding author email address: albert.queralto.lopez@gmail.com
Electronic Supplementary Information (ESI) available: HAADF simulations, surface energies of CGO facets, and dependence of the lateral aspect ratio with the heating rate and temperature.
See DOI: 10.1039/x0xx00000x

Please do not adjust margins

Please do not adjust margins

furnaces is the most extended fabrication tool of CSD. However, they are limited to slow heating ramps; thus, a detailed study of nucleation and coarsening phenomena is precluded since they can occur almost simultaneously, and nucleation and growth rates are often temperature dependent. Instead, rapid thermal annealing (RTA) furnaces use very fast heating ramps of tens of ºC s^{-1}, and can reach temperatures as high as 1200 ºC. In addition, they provide a precise control over the annealing temperature, with a small error (~0.1 ºC) and a small overshoot (~1 ºC) at high temperatures. Thus, RTA appears as very adequate tool to combine with CSD to conduct a detailed study of nucleation and coarsening phenomena. RTA has been mainly used during semiconductor processing to implant ions and make electrically active dopants with minimal diffusive motion[40] or to obtain high concentration of dopants in the channel under the gate in CMOS.[41, 42] Some examples of its application for CSD-based materials are the growth of multi-layered architectures to develop fully functional oxide thin-film capacitors with good ferroelectric and fatigue properties,[43] as well as, oxide electrodes with low resistivity.[44] The fast heating ramps developed by RTA can also be used to select or avoid the formation of phases present during oxide thin-film growth such as the pyrochlore phase in $Pb(Zr_xTi_{1-x})O_3$.[45] Nevertheless, few studies have reported the fabrication of epitaxial layers by means of RTA such as $Pb(Zr_xTi_{1-x})O_3$, $La_2Zr_2O_7$ or our recent investigations on $Ce_{1-x}Zr_xO_{2-y}$, $LaNiO_3$ and $Ba_{0.8}Sr_{0.2}TiO_3$ films.[46-49] Nanostructures from oxides such as $Ce_{1-x}Gd_xO_{2-y}$, $Pb(Zr_xTi_{1-x})O_3$ and $La_{0.7}Sr_{0.3}MnO_3$ have also been grown by CSD and CTA.[11, 12, 14, 15, 50-52] However, the use of RTA will likely provide a better understanding of the nucleation and coarsening mechanisms involved, particularly for complex oxide systems where two or more cations are present which could derive in the nucleation of different phases.

The ability to control the growth of nanostructures is essential in order to fabricate devices where the compelling functional properties depend on the particular crystalline orientation.[15, 53-55] Previously, we reported on the growth of $Ce_{1-x}Gd_xO_{2-y}$ (CGO) nanostructures on (001)$LaAlO_3$ (LAO) substrates by CSD and CTA treatments.[14, 50, 51] Two different morphologies, linked to dissimilar crystalline orientations and interfacial growth states, were stabilized depending on the growth conditions, i.e. oxygen partial pressure and temperature. We obtained the (001)CGO[110]||(001)LAO[100] orientation with an isotropic shape, i.e. nanodots (NDs), when annealing in oxygen atmosphere. A labyrinthine structure of orthogonal nanowires (NWs) with two equivalent in-plane orientations (011)CGO[100]||(001)LAO[100] and (011)CGO[110]||(001)LAO[010] was formed when annealing under Ar-H_2.[50] Additionally, it has been demonstrated that nanoscratching is also very practical to achieve direct self-assembling of CGO nanowires grown by CSD.[56] These nanostructures are ideal to investigate the low energy and highly oxygen deficient {111} lateral facets which have attracted great interest for catalysis, gas sensors and ionic conductivity applications.[54, 57-61] For example, they could potentially be good candidates for the fabrication of bridge sensing architectures. Furthermore, we will see that NWs elongate along the direction with {111} lateral facets and, hence, they push forward new ways to develop and investigate these widely used facets. In this work, we employ fast RTA treatments to grow self-assembled (011)CGO NWs on (011)LAO substrates oriented along a single substrate orientation, thus, breaking the biaxial symmetry previously obtained. Systematic investigations allow the evolution of morphology, orientation and structure of NWs to be evaluated, as well as their oxidation state. Thermodynamic and 3D atomic models are also used to complete the study, predicting and establishing the final stable morphology, strain state and kinetic behavior of the NWs.

The fabrication methodology and theoretical analyses presented will prove ideal for the understanding of the thermodynamic and kinetic mechanisms involved in the nucleation and coarsening of oxide nanostructures. They have demonstrated useful in different interfacial nanostructures and could also be systematically applied to a broad range of ex-situ grown materials by taking into account the particular combination of facets, and surface and strain energies.

2 Experimental

We have grown heteroepitaxial $Ce_{0.9}Gd_{0.1}O_{2-y}$ (CGO, a_{CGO}=0.541 nm) NWs by CSD on 0.5 mm-thick 5x5 mm^2 (011)$LaAlO_3$ (LAO, a_{LAO}=0.379 nm) single crystal substrates (Crystec). Ultra-diluted solutions are prepared from Cerium (III) and Gadolinium (III) acetylacetonates (Sigma-Adrich) mixed in propionic acid. The concentrations of Ce and Gd are properly adjusted to get the desired stoichiometry. Subsequent stirring and heating at 50 ºC for 30 min leads to dissolution of the compounds and the formation of cerium – gadolinium propionates with a total metal ion concentration of 0.25 M. Then, the solution is diluted by addition of propionic acid until the concentration is 0.008 M and, finally, it is filtered with a 0.2 µm to eliminate any impurities. Prior to deposition, the substrates are cleaned with acetone and methanol in ultrasonic bath, and annealed at 900 ºC during 5 h under O_2 to obtain atomically flat terraces. Afterwards, we spin 14 µl of solution on each substrate (6000 rpm, 3000 rpm·s^{-1}, 2 min). A two-step growth procedure is used in our experiments: 1) The pyrolysis of the metal-organic film obtained after spin-coating using a tubular furnace at 300ºC for 15 min, deriving in the transformation of the propionates film into a homogeneous nanocrystalline layer.[62] 2) The growth of NWs is carried out in a RTA system (AS-Micro from Annealsys) under controlled conditions (atmosphere, temperature and heating rate) at a maximum temperature of 1100ºC in oxygen for variable dwell times and heating rates.

Atomic Force Microscopy (AFM, Agilent 5100 system from Agilent Technologies) is used in tapping mode at room temperature and atmospheric pressure to investigate NWs topography. Analysis of topographic images is done with Mountains Map 7.0 software (Digital Surf). Two-dimensional X-ray diffraction (XRD^2) pole figures are carried out in a GADDS D8 Advance system from Bruker to determine the crystalline orientation of NWs. ϕ-scans are obtained in 180 steps of 2º at specific 2θ-χ regions; holding each position for 40 s to collect enough signal. The pole figure is built integrating over a specific 2θ angle. The χ position of the resulting diffraction peaks enables us to determine the in-plane crystallographic orientation of the interfacial nanostructures.

Scanning Transmission Electron Microscopy (STEM) experiments are performed to analyze the crystalline structure and morphology of the NWs, including their orientation, epitaxial relationship with the substrate and their faceting.

 This journal is © The Royal Society of Chemistry 20xx

Please do not adjust margins

Please do not adjust margins

Specimens are prepared by conventional mechanical polishing and Ar-ion milling. High Angle Annular Dark Field (HAADF) or Z-contrast images are obtained in a probe corrected FEI Titan 60-300 operated at 300 keV. From the HAADF-STEM atomic resolution images, we obtain the structural data to create 3D atomic models of the CGO NWs epitaxed on the LAO substrate. The models have been created by using the Rhodius Software,[63] which allows creating complex atomic models,[30, 64] including nanowire-like structures.[65, 66]

Reflection high energy electron diffraction (RHEED) is performed with a Staib Instruments system using an electron beam of 30 kV, a current of 50 µA and incidence angles between beam and sample surface below 2º. The investigated incident directions are the <100> and <110> substrate orientations. Additionally, the diffraction pattern is simulated with a software based on the kinematic theory of electron scattering.

X-ray Photoelectron Spectroscopy (XPS) measurements are performed in an ultra-high vacuum (UHV) chamber with a base pressure of 10^{-10} mbar. The plane of the surface is kept at 60º with respect to the hemispherical analyzer (Specs-PHOIBOS100). The X-ray radiation corresponds to the Mg Kα line (1253.6 eV). Narrow scans of Ce 3d core level are recorded using a pass energy of 15 eV with energy steps of 0.1 eV. Up to 330 scans are accumulated for each measurement to decrease the signal-to-noise ratio at the Ce 3d core level spectra since the proportion of Ce in the sample is very small (around 2% on the wide scan). The contribution of Mg Kα satellite lines is subtracted and the background removed by a Shirley routine prior to XPS data evaluation. The analysis of the Ce 3d core level peak is performed according to Romeo *et al.*[67] All the XPS measurements are carried out *ex-situ*.

3 Results and discussion

3.1 Morphology, structure and stoichiometry of nanowires

Heteroepitaxial CGO nanowires (NWs) have been grown on (011)$LaAlO_3$ (LAO) substrates from ultradiluted precursor solutions. Growth heating ramp (0.5-20 ºC s^{-1}), temperature (800-1100ºC) and annealing time (0-15 min) are varied in order to investigate nucleation and coarsening. The study of precursor films is mandatory in order to understand the mechanisms leading to the formation of CGO NWs on (011)LAO substrates. For instance, the initial organic precursor is known to influence the pyrolysis process, as well as the crystallization kinetics as demonstrated previously by Rupp et al.; and this could be of relevance for CGO NWs.[68, 69] We have performed RHEED measurements of CGO precursor films pyrolyzed at 300 ºC for 30 min in oxygen on (011)LAO substrates (**Figure 1a**). We observe a diffuse halo which indicates the presence of amorphous content. The bright spot in the halo with some additional faint ones on a half circle correspond to the (011)LAO substrate (**Figure 1b**) as the depth information is about 5 nm, whereas the precursor film has a thickness of ~2 nm, as we will see later. Additionally, the halo is not completely featureless, which may indicate the presence of some nanocrystalline material. Equivalent investigations have been done for comparison purpose on (011)CGO NWs annealed at 1000 ºC for 5 min which show a characteristic CGO diffraction pattern (**Figure 1b**). **Figure 1c** presents a more local investigation with HRTEM of the CGO precursor films. We see that the CGO precursor film has a thickness of 2 nm and already presents uniaxial (011)CGO nanograins as evidenced from the Fourier-filtered TEM image and hinted from RHEED measurements. The film surface is very smooth with a RMS roughness below 0.5 nm as seen in **Figure 1d**. Pyrolyzed CSD-derived precursor oxide films are usually amorphous as reported for lead-based oxides.[38, 70] Alternatively, some oxides such as barium/strontium titanates may experience a transition from intermediate oxide phases to the final oxide under certain conditions.[38, 70] However, our results show the presence of the final CGO structure at very low temperatures. A previous study from Roura et al. has also demonstrated the formation of nanocrystalline ceria films from propionate precursors after annealing at 200 ºC for 1 h.[62] This seems to indicate that CGO has a large driving force to nucleate the final phase without transitioning to intermediate phases. In order to further minimize the nucleation of CGO nanograins at such low temperatures, we reduced the pyrolysis time to 10 min.

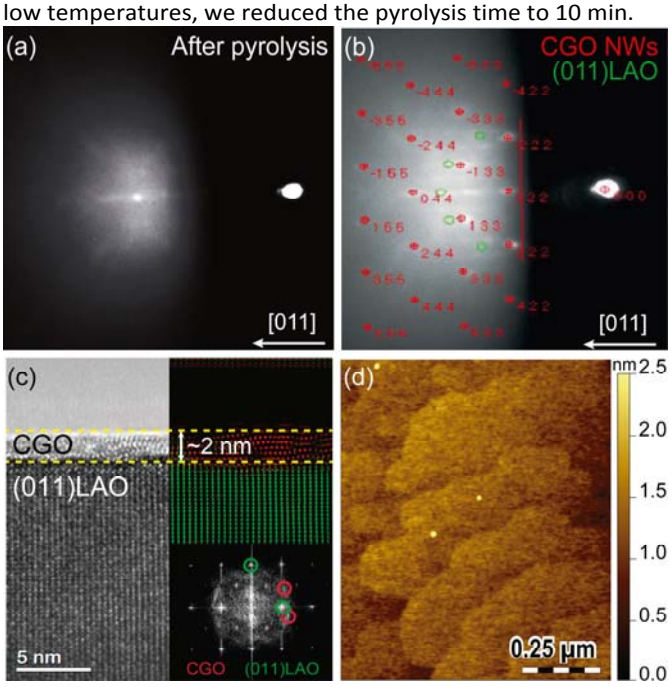

Figure 1. RHEED measurements of (011)CGO on (011)LAO: (a) pyrolyzed CGO precursor film after 30 min at 300 ºC in O_2, and (b) (011)CGO NWs grown at 1000 ºC, 20 ºC s^{-1} for 5 min in O_2. The spots marked in red (CGO NWs) and green (LAO substrate) were recalculated with a software based on the kinematic diffraction theory. (c) HRTEM image and corresponding FFT of the pyrolyzed CGO precursor film on (011)LAO. (d) AFM image of the surface morphology.

Figure 2a presents the topographic AFM image of a sample grown at 1000ºC, 20 ºC s^{-1} for 15 min in O_2. The formation of self-assembled parallel CGO NWs is completed at short annealing times since there is no remaining material on the substrate steps. This also reveals a full conversion from the initial nanocrystalline film into epitaxial nanostructures. The NWs presented have heights between 5 and 10 nm, widths up to 30 nm and lengths as large as 650 nm, meaning that high aspect ratios can be obtained (length/width=20 and length/height=100) with estimated effective growth rates between 10 and 40 nm min^{-1}. We also observe the presence of small isotropic islands which will be studied later. **Figure 2b** shows the length profile of a single nanowire with a height of 9 nm and a length of 450 nm approximately. XRD^2 pole figures of the LAO substrate and CGO NWs (**Figure 2c** and **2d**) indicate that the CGO NWs grow with a (011) out-of-plane orientation.

Please do not adjust margins

Please do not adjust margins

In addition, the substrate notches seem to indicate that the direction of enlargement should correspond to the [0-11]CGO, as it will be confirmed later by STEM. Compared to the NWs previously grown on LAO(001) and distributed along two orthogonal in-plane directions,[50] NWs grown on (011)LAO are arranged along one single orientation breaking the degeneracy observed on (001) substrates (vertically displayed in **Figure 2a**). The underlying mechanisms of this phenomenon will be discussed in section 3.2.

The nanowires have been observed by atomic resolution HAADF STEM along two orthogonal directions, as shown in **Figure 3**. Samples are analyzed from the [100]LAO zone axis, allowing the visualization of NWs along the [0-11]CGO (frontal or cross-section view, **Figure 3a** and **3b**) and, also, from the [0-11]LAO axis, offering a lateral view of the NWs, where the CGO is observed from the [100] direction (lateral or longitudinal view, **Figure 3c, 3d** and **S1**). CGO NWs are well faceted by low index planes; {111} planes define the wire borders in the [0-11]CGO

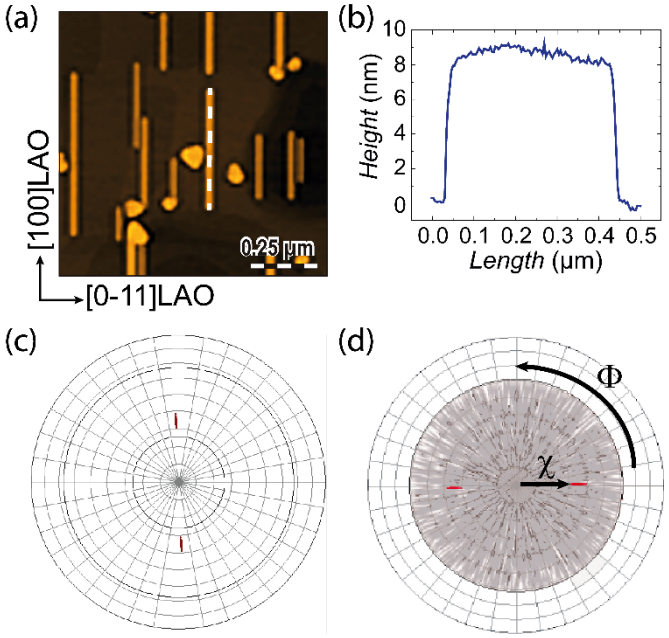

Figure 2. Self-assembled parallel (011)CGO nanowires grown on (011)LAO single-crystal substrates at 1000 ºC in O_2 atmosphere. (a) AFM topographic image of CGO nanowires annealed for 15 min, 20 ºC s^{-1}, and (b) a representative profile of a single nanowire of 450 nm in length and 9 nm in height. XRD^2 pole figures centered at the (111) Bragg reflection of (c) a (011)LAO substrate, and (d) (011)CGO NWs. The background color in (d) has been changed for more visibility of poles.

projection (frontal view model**, Figure 3f**), i.e. the large dimension, while {010} planes do it along the [100]CGO projection (lateral view model, **Figure 3g**), i.e. the short dimension. The growth plane of CGO NWs is the (011), as can be extracted from the fast Fourier transforms (FFTs) included in **Figure 3b** and **3d**. Thus, under the presented experimental conditions, the CGO structure grows on the (011)LAO substrate showing the epitaxial relationship: (011)CGO[0-11]||(011)LAO[100]; and presenting an in-plane rotation of 90º between both structures. The theoretical lattice mismatch ε of CGO NWs with the (011)LAO substrate is evaluated along the short and long axes ($\varepsilon = [d_{LAO} - d_{CGO}]/d_{CGO}$, where d_{LAO} and d_{CGO} are the matching distances of the LAO substrate and CGO NWs, respectively). The calculation reveals a very low mismatch of -1% for both in-plane directions, also confirmed by TEM. Thus, low-misfit epitaxy (LME), which considers the matching of the same planes or lattice parameters if the misfit is smaller than 7-8 %, is the model to be applied. This is in contrast with NWs grown on (001)LAO which show two strain states: low lattice mismatch of -1% along the [011]CGO//[010]LAO direction, being able to apply LME, while a very high mismatch of -30% was found along the [100]CGO//[100]LAO direction if LME is used. However, it was demonstrated by TEM that the domain matching epitaxy (DME) model, which considers the matching of different planes and interplanar distances along different directions, was more suitable than LME in order to describe the structure better and obtain a reduced mismatch of 5%.[50]

The presence of oxygen vacancies in CeO_2 nanomaterials has been linked to the fast growth kinetics observed.[50, 51] Thus, the oxygen stoichiometry of (011)CGO NWs on (011)LAO has been investigated by evaluating the oxidation state of Ce ions. **Figure 4** shows the XPS Ce 3d core level spectrum of the NWs grown in O_2. The spectrum is composed of six peaks associated to Ce^{4+} (shaded in red) and four peaks from Ce^{3+} (shaded in green). The quantification of both Ce ions, from deconvolution of the core level spectrum following the procedure reported elsewhere,[67] allowed us to determine a ratio Ce^{3+}/Ce^{4+}(%) = 40/60. This ratio is equivalent to that reported for (001)CGO NDs grown on (001)LAO in O_2 (Ce^{3+}/Ce^{4+}(%)=40/60), whereas it is significantly smaller than the ratio observed for (011)CGO NWs grown on (001)LAO in Ar-H_2 (Ce^{3+}/Ce^{4+}(%)=65/35).[51] The content of oxygen vacancies has been proposed to depend on CeO_2 surface facets. In particular, a DFT study by Branda et al. suggests that the formation energy of oxygen vacancies depends on the facet, being the low Miller index facets, i.e. {111}, {110} and {100}, those with higher oxygen reduction potential.[55] Hence, the large amount of vacancies in our NWs. It has also been suggested that the reduced oxygen content of (011)CGO NWs on (001)LAO could be caused by their complicate interface, as well as the Ar-H_2 annealing ambient.[14, 50, 51] Furthermore, ceria nanostructures are quite robust since they can sustain a large amount of oxygen vacancies maintaining the fluorite structure. Equivalent XPS measurements of 20-nm thick CGO films grown in O_2 reveal no Ce^{3+} ions.[71] Although XPS is a good technique to measure the oxidation state, it can only sense around 30% of the sample due to thickness and electron mean free path limitations. Thus, other techniques have been used in the literature to evaluate oxygen vacancies. STEM-EELS experiments on CeO_{2-x} nanoparticles (NPs) have suggested that small-sized NPs are fully reduced (Ce^{3+}/Ce^{4+}(%)=100), while NPs with larger dimensions present a distribution of oxygen vacancies across the surface.[72-76] Song *et al.* have also reported oxygen vacancies by STEM-EELS at the interface of CeO_2 films grown on (111)YSZ substrates by PLD.[77] We have conducted

This journal is © The Royal Society of Chemistry 20xx

Please do not adjust margins

Please do not adjust margins

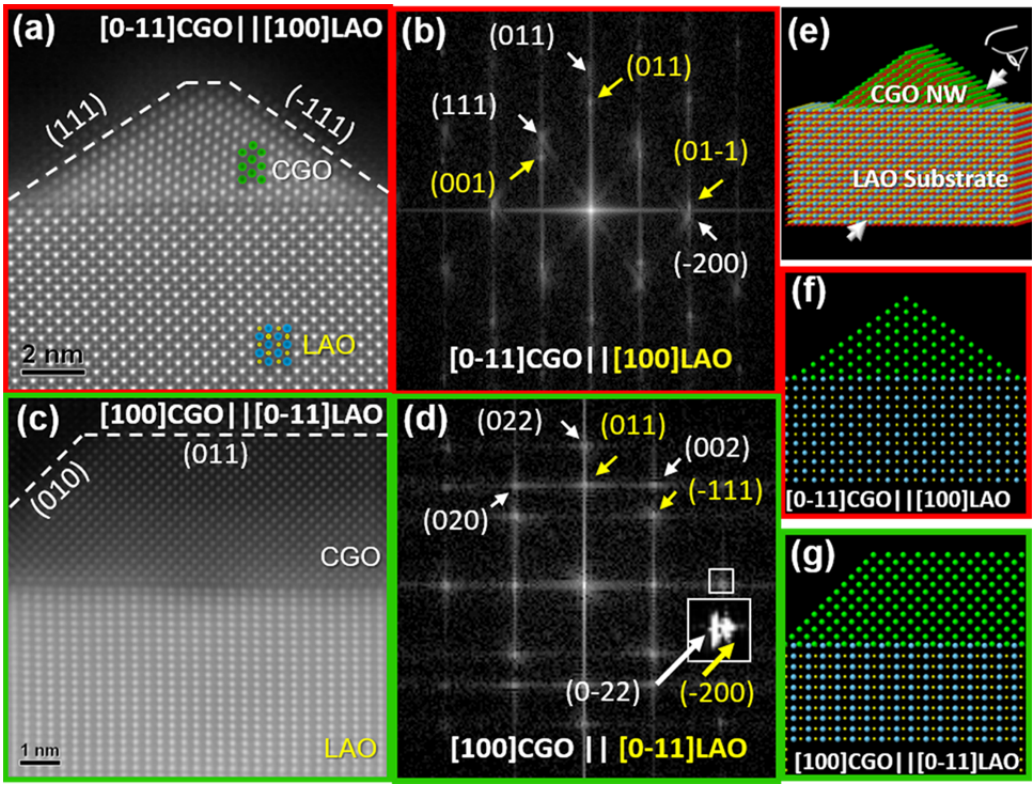

Figure 3. (a) Cross-sectional HAADF STEM image of a (011)CGO nanowire (front view) viewed from the [0-11]CGO//[100]LAO zone axis. (b) Power spectrum obtained from the HAADF STEM image in (a). (c) Cross-sectional HAADF STEM image of a (011)CGO nanowire (lateral view, longitudinal) viewed from the [100]CGO//[0-11]LAO zone axis. (d) Power spectrum obtained from the HAADF STEM image in (c). (e) 3D atomic model of a CGO NW on a LAO substrate, and corresponding (f) front and (g) lateral views.

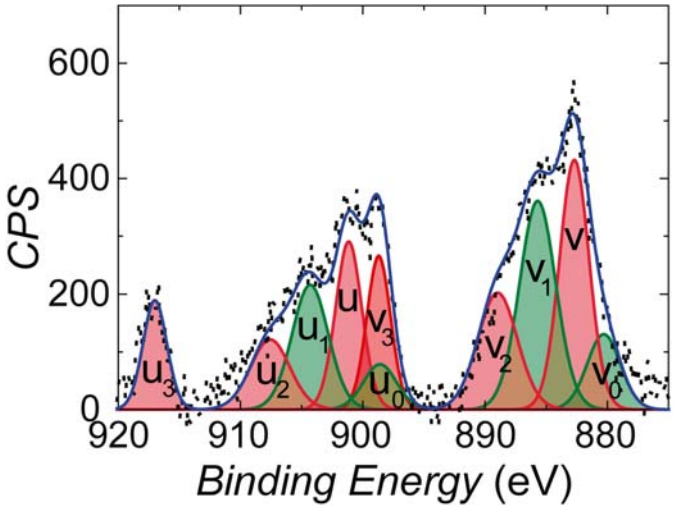

Figure 4. XPS Ce 3d core level spectrum of (011)CGO nanowires grown on (011)LAO substrates by RTA at 1000 ºC, 20 ºC s^{-1} for 5 min in O_2 atmosphere. The fitted components in green and red correspond to Ce^{3+} and Ce^{4+} ions, respectively.

equivalent measurements on CGO NDs which suggest the presence of a large amount of oxygen vacancies along them.[48] However, no decisive results have been obtained since sample preparation by PIPS or electron beam interactions during the measurements could be modifying the oxygen content as reported in Ref [78]. Solovyov *et al.* have also evaluated the amount of oxygen vacancies through the analysis of reciprocal space maps acquired with synchrotron X-ray diffraction.[79] The analysis of symmetric and asymmetric reflections has revealed that oxygen vacancies are distributed inhomogeneously along CGO NDs with a high concentration at the interface. These results are also consistent with the large amount of oxygen vacancies reported by Garcia-Barriocanal *et al.* at the interface of YSZ/STO epitaxial heterostructures.[80] This phenomenon may not be exclusive of CGO NDs, and it could play a vital role in the structural relaxation of NWs. Therefore, we hypothesize that the interface between nanoislands and substrate, their small dimensions and the island facets may be responsible for determining the amount of oxygen and its distribution inside the CGO structure. A feasible explanation for this issue could be ascribed to the larger surface-to-volume ratio of nanoislands as compared to thin-films, which favors a fast oxygen depletion. The presence of different chemical terminations may also influence the formation of oxygen vacancies as suggested before.[73] Nevertheless, it is still an open issue requiring further investigation.

3.2 Thermodynamic model and broken degeneracy of nanowires

The stable shape of CGO NWs is elucidated by applying a model similar to that reported by Gibert *et al.*[81] In general terms, we suppose that the rapid formation of self-assembled nanoislands is thermodynamically governed and, thus, allows the model to be applied. Accordingly to our TEM results, we assume a trapezoidal-prismatic shape with height *h*, short axis *a*, and long axis *b* (**Figure 5a**). Lateral facets corresponding to the short axis are tilted at an angle δ with respect to the substrate, while long axes' facets are slanted an angle ϑ. A truncated island is considered since this is the most commonly seen shape for (011)CGO NWs (**Figure 3a**).[50]

The energy required to form a nanowire is mainly composed by

Please do not adjust margins

Please do not adjust margins

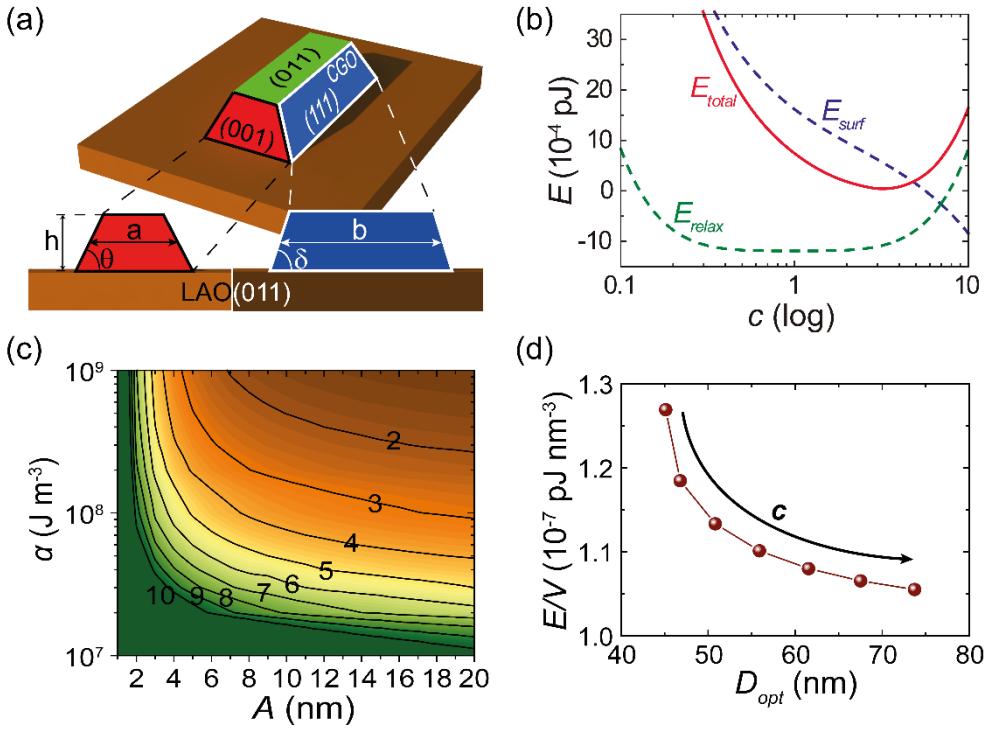

Figure 5. (a) Schematic representation of the considered island shape in the thermodynamic model. Phase diagrams and energy calculations of interfacial (011)CGO NWs on (011)LAO substrates: (b) $E_{total}(c)$ (red solid line), $E_{surf}(c)$ (blue dashed solid line), and $E_{relax}(c)$ (green dashed line) corresponding to a specific island size. Parameters used for the plot are D=40 nm, h=4 nm, α=10^8 J m^{-3}, β=1 and A=5.5 nm. (c) Contour plot showing the dependence of equilibrium lateral aspect ratio c_{eq} with respect to A and α (D=40 nm and h=5 nm). (d) Energy per unit volume E/V as a function of D_{opt} for different lateral aspect ratios (h=4 nm, α=10^8 J m^{-3}, β=1 and A=4.4 nm). We show the growth direction of the lateral aspect ratio c.

the contribution of the surface energies of the external facets and the elastic relaxation energy associated with the interfacial misfit strain. Thus, it can be written as:

$$E = E_{surf} + E_{relax} + E_{edges} \quad (1)$$

where E_{surf} corresponds to the surface energy, E_{relax} to the elastic relaxation energy, and E_{edges} to the short-range contribution of the edges.[82] The change in total energy can be expressed, without considering the effect of the edges, in terms of the *effective diameter* $D=(ab)^{1/2}$ and *lateral aspect ratio* $c=(b/a)^{1/2}$ as:

$$E_{total} = \underbrace{\Psi D^2 - \Phi h D\left[c\cot\theta + \frac{1}{c}\cot\delta\right] + 2hD\left[\frac{\gamma_b c}{\sin\theta} + \frac{\gamma_a}{c\sin\delta}\right]}_{E_{surf}} \underbrace{-\alpha h^2 D\left\{\frac{1}{c}\ln\left(\frac{cD}{A}\right) + \beta c\ln\left(\frac{D}{cA}\right)\right\}}_{E_{relax}} \quad (2)$$

where in the first term of the equation, corresponding to E_{surf}, γ_a and γ_b are the surface energies of short and long lateral facets, respectively, and $\Psi \equiv \gamma_t + \gamma_i - \gamma_s$ and $\Phi \equiv \gamma_t - \gamma_i + \gamma_s$, with γ_s, γ_t and γ_i being the surface energies of the substrate, top facet of the island, and the substrate-interface energy, respectively. In the second term, corresponding to E_{relax}, $\alpha = \sigma^2(1-\nu)/\pi\mu$, σ is the island stress tensor which depends on the Young modulus and misfit strain, υ and μ the Poisson's ratio and shear modulus of the substrate, and A is a parameter proportional to the island's height and properly renormalized to incorporate the geometry of the edges.[82-84] Additional values for these parameters can be found in **Table S1** (Supporting Information) and are also reported elsewhere.[48, 81, 85, 86] In the calculation of the elastic relaxation energy, the corrective factor β considers the in-plane biaxial strain anisotropy that could be present in some cases. However, as reported before, there is no such strain anisotropy in the present system, (001)CGO[0-11]||(011)LAO[100], which means that β=1 leading to the same equation derived by Tersoff and Tromp.[84] **Figure 5b** illustrates the $E(c)$ dependence and its energetic contributions (E_{surf}, E_{relax}) for a (011)CGO NW on (011)LAO. Notice that E_{surf} decreases when the lateral aspect ratio increases. This means that the contribution of the surface energy promotes the continuous elongation due to the different orientation of lateral facets and, thus, the different surface energies associated. On the other hand, E_{relax} favors isotropy and does not contribute to the elongation.

The dependence of the lateral aspect ratio c with A and α (**Figure 5c**) allows us to evaluate the different energy contributions to the overall island energy. In fact, α and A weigh the contribution of the elastic relaxation energy to the E_{total}. So, for high α and A values the weight of E_{relax} becomes more important and c gets close to the isotropic nanoisland value (c=1). When both parameters decrease, c increases indicating that the importance of E_{relax} is reduced and E_{surf} dominates the whole island energy, favoring nuclei with high aspect ratios.

A differentiating aspect of the present (011)CGO system is that the energy minimum appears at an aspect ratio c>1 (**Figure 5b**). Since the elastic relaxation energy is isotropic, the reason of that behavior resides in the dissimilar surface energies of nanowire's facets that act as the driving force for the

Please do not adjust margins

Please do not adjust margins

formation of islands with an elongated shape. The spontaneous formation of NWs is triggered by unrestricted coarsening along one direction. In order to address that, we must consider the change of energy as the size of the island increases. For that purpose, we study the dependence of the energy per unit volume (i.e. energy density) (*E/V*), being $V \sim hD^2$, with the optimum island size D_{opt} which is the diameter having a minimum of *E/V* for a given lateral aspect ratio *c*. **Figure 5d** shows a decrease of nanowires' *E/V* with D_{opt}, indicating that the formation of long NWs is favored thermodynamically. Nevertheless, it is still unknown why the growth kinetics is sufficiently fast to promote the formation of nanostructures with the predicted equilibrium elongated shapes. Additionally, it is unclear why NWs' configuration is parallel, thus, different hypothesis could be made. A plausible explanation is that, due to an existing high strain configuration, the "other" orientation is either unable to nucleate (high nucleation barrier) or remains as isotropic islands (**Figure 2a**). HRTEM and HAADF-STEM investigations (**Figure 6a-c**) reveal that these isotropic islands have a truncated pyramid-like shape with the same low strain and epitaxial arrangement with the substrate to that of (011)CGO NWs on (011)LAO, i.e. (011)CGO[100]//(011)LAO[0-11].

If we assume that the variation of the Gibbs free energy in our system is:[41, 47, 77]

$$\Delta G(D) = -hD^2(\Delta G_v - \Delta G_{str}) + \Psi D^2 + \Gamma Dh \qquad (3)$$

where $\Delta G_v = \Delta\mu/v$ is the Gibbs free energy per unit volume, v is the unit cell volume, $\Delta\mu(>0)$ is the change in chemical potential or supersaturation between the epitaxial and amorphous/nanocrystalline state, ΔG_{str} is the misfit strain energy per unit volume, and $\Gamma = [2(\gamma_b c \csc\theta + \gamma_a c^{-1}\csc\delta) - \Phi(c\cot\theta + c^{-1}\cot\delta)]$.

Then, the nucleation barrier as a function of the supersaturation and strain (G^*_{str}) can be written as:[48]

$$G^*_{str} = \frac{-\Gamma^2 h^2}{4\left[-h\left(\frac{\Delta\mu}{v} - \Delta G_{str}\right) + \Psi\right]} \qquad (4)$$

Figure 6d shows the evolution of the nucleation barrier of CGO nanowires with the supersaturation for different values of $\Delta G_{str}\left(0, \frac{\Delta\mu}{v}, \frac{3\Delta\mu}{v} \text{ and } \frac{5\Delta\mu}{v}\right)$. Considering that $\Delta G_{str} \sim \Delta\mu/v$ for (011)CGO NWs, any other orientation with higher strain will have a larger nucleation barrier for a specific value of supersaturation. The other arrangements between the CGO and LAO structures would be [100]CGO||[100]LAO and [0-11]CGO||[0-11]LAO with biaxial strains of -30% in both directions. Hence, it is highly probable that configurations with such large strain are unable to nucleate on (011)LAO substrates at the present experimental conditions due to their high energy barrier and the low strain energy of the orientation nucleated in this study.

3.3 Fast kinetics and coarsening of nanowires

It has been mentioned that the fast heating ramps achieved by RTA furnaces allow us to select and analyze specific points of the growth process, and thus, study the kinetic evolution of NWs. Several coarsening mechanisms can occur simultaneously during the growth of nanoislands.[87] We can identify conventional Ostwald ripening, which is related to diffusion of atoms between NWs. Static coarsening is also observed, which accounts for the growth of islands that do not translate but grow from supersaturation when they are in contact; seeing that nanowires tend to increase their size at expenses of the neighboring ones.

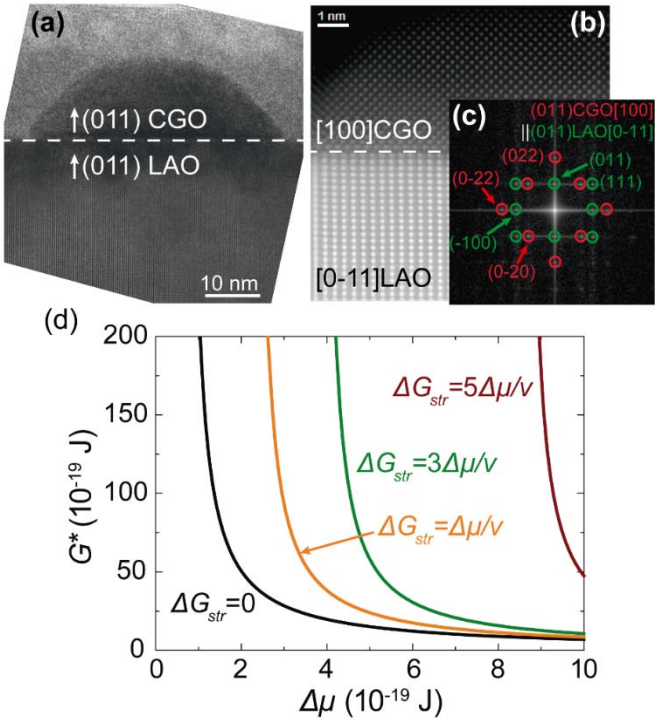

Figure 6. (a) HRTEM image of a short length (011)CGO island on (011)LAO. (b) HAADF-STEM characterization, and (c) power spectrum of an equivalent island viewed from the [100]CGO//[0-11]LAO zone axis. The sample was grown at 1100 ºC, 20 ºC s^{-1} for 5 min in O_2. (d) Dependence of the nucleation barrier (G^*) with the supersaturation ($\Delta\mu$) for different strain contributions (ΔG_{str}).

Figure 7a and **7b** show the AFM images of two different RTA experiments at 1000 and 1100 ºC with a heating rate of 20 ºC s^{-1} and no dwell time, while **Figure 7c** and **7d** present the AFM images of NWs grown at 1000 ºC and heating ramps of 5 and 0.5 ºC s^{-1}. It is seen that NW dimensions increase with temperature and by slowing the heating ramp. A more detailed

study is depicted in **Figure 7e** where we see that the mean volume increases from 800 to 4000 nm^3 as the heating ramp is decreased. This indicates that the influence of coarsening is small at fast heating ramps, thus, allowing a much precise investigation of coarsening. Furthermore, we demonstrate that the influence of coarsening in previous investigations where conventional thermal annealing was used, i.e. heating ramps slower than 0.5 ºC s^{-1}, was significantly large. Hence, nucleation and coarsening must be studied at heating ramps as fast as 20 ºC s^{-1} in order to separate both contributions sufficiently. Despite that, the increase in volume with temperature reveals that the influence of coarsening cannot be excluded completely at very high temperatures, i.e. 1100 ºC, where the volume is comparable to that of slow heating ramps. The dependence of the lateral aspect ratio *c* at heating rates from 20 to 0.5 ºC s^{-1} and temperatures from 900 to 1100 ºC (**Figure S2**) indicates that the main increase in volume comes from the growth of NWs along their length, confirming what we predicted from thermodynamic calculations. The temperature dependence of island dimensions can be attributed to the enhanced atomic mobility achieved at high

Please do not adjust margins

Please do not adjust margins

temperatures leading to a boost in the diffusion of atoms between NWs. Large atomic mobility has also been reported in other CSD cases, where a transition between thin-film morphology to nanostructures has been observed by rising the annealing temperature.[88]

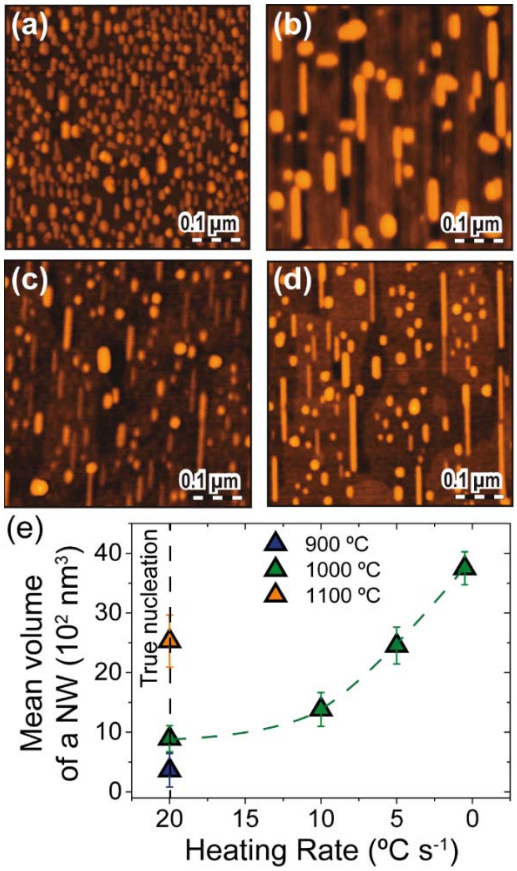

Figure 7. AFM images of nanowires grown on (011)LAO substrates in O_2 without dwell time at: (a) 1000 ºC, 20 ºC s^{-1}, (b) 1100 ºC, 20 ºC s^{-1}, (c) 1000 ºC, 5 ºC s^{-1} and (d) 1000 ºC, 0.5 ºC s^{-1}. (e) Dependence of the mean volume of a NW with the heating rate and temperature, extracted from AFM images (a-d). The black dashed vertical line indicates the heating rate where the contribution of coarsening is considered to be negligible.

Figure 8a and **8b** show the increase in size between samples annealed at 1000 ºC and 20 ºC s^{-1} for 0 and 15 min. **Figure 8c** plots the mean volume of a single NW for additional samples annealed at 1000 ºC and 20 ºC s^{-1}. This allows us to visualize an enhanced isothermal growth of NWs' volume. We can approximately extrapolate a coarsening velocity (v_c) of ~14 nm min^{-1}. This coarsening rate is rather fast considering that ripening of nanoislands by the mechanisms described before should be much slower as they have a thermodynamically stable equilibrium size. Some works have observed an enhancement of the Ostwald ripening by elastic repulsive interactions between nanoislands.[87] The inset in **Figure 8b** shows that some NWs keep a very close distance between them (few nanometers) without experiencing coalescence. This may be indicative of the presence of repulsive interactions. Furthermore, the large amount of oxygen vacancies present in the NWs could have an important influence in their enhanced kinetics and, hence, lead to fast coarsening rates. Similar coarsening phenomena have been considered previously for the orthogonal NWs.[50] In addition, we also reported the presence of dynamic coalescence, which consists in the diffusion of nanoislands as a whole. This coalescence mechanism is associated to attractive interactions between different island facets {111} and {100}, and it is caused by the orthogonal configuration of CGO NWs grown on (001)LAO substrates. Since the present NWs are arranged parallel, they do not meet this condition and, therefore, no attractive interactions have been identified to affect their coarsening behavior.

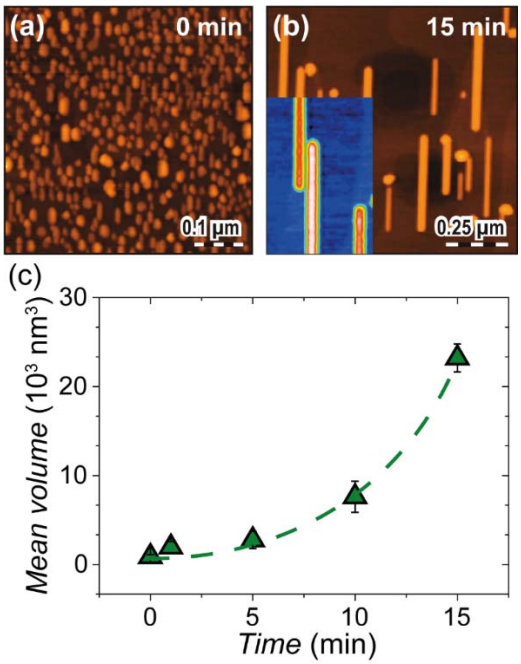

Figure 8. AFM images showing the evolution of nanowires grown in O_2 at 1000 ºC: (a) 0 min, and (b) 15 min of annealing. Inset: two close NWs illustrating the presence of elastic repulsive interactions. (c) Evolution of the mean volume of a single NW with time from 0 to 15 min.

Conclusions

Tuning the strain configuration between CGO NWs and substrate allows selecting between two different self-organized arrangements, i.e. a single orientation of parallel NWs are obtained when grown on (011)LAO substrates (present study), whereas orthogonal NWs have been grown on (001)LAO substrates (previous works). An extremely fast bottom-up methodology has been employed to spontaneously grow (011)CGO NWs by CSD and RTA furnaces with estimated growth rates between 10 and 40 nm min^{-1}. The epitaxial relationship between NWs and the substrate is (011)CGO[100]||(011)LAO[0-11], i.e. CGO and LAO structures are rotated 90º in-plane. CGO NWs on (011)LAO substrates grow following a LME model, which enables the growth of biaxially isotropically strained NWs with a low strain configuration of -1%. In contrast, NWs on (001)LAO substrates followed the DME model due to the anisotropy in strain. The anisotropy observed in the surface energy is then the main contribution to the formation of thermodynamically stable and elongated NWs after nucleation. The large nucleation barrier for high strain configurations completely discards the

This journal is © The Royal Society of Chemistry 20xx

Please do not adjust margins

Please do not adjust margins

formation of nanostructures with -30 % biaxial strain, and thus, (011)CGO nuclei which end forming parallel NWs are presented as the only possible morphology on (011)LAO substrates. Thermodynamic calculations show a decrease in the energy per unit volume as the lateral aspect ratio increases which seems to indicate that NWs' should elongate indefinitely. Experimental results confirm the enhanced growth of NWs along their length.

The oxidation state of (011)CGO NWs on (011)LAO substrates, i.e. Ce^{3+}/Ce^{4+}(%)=40/60, has been found to be equivalent to that of (001)CGO isotropic nanoislands on (001)LAO substrates, both grown in oxygen atmosphere. Instead, NWs grown on (011)LAO in Ar-H_2 have a ratio Ce^{3+}/Ce^{4+}(%)=65/35, which indicates that the islands facets, the interface between CGO nanostructures and the LAO substrate, the annealing atmosphere and the dimensionality of our NWs highly determine the amount of oxygen vacancies in the CGO structure.

We demonstrated that nucleation and coarsening can be separated when using fast heating ramps, only available with RTA furnaces. Kinetic mechanisms such as conventional Ostwald ripening modified by elastic repulsive interactions, static coarsening and enhanced coarsening due to oxygen vacancies are likely contributing to the very fast growth rates between 10 and 40 nm min^{-1}. In summary, our investigations reveal that the direction of NWs' elongation is the one with {111} lateral facets which also possesses a large amount of oxygen vacancies, and it has the lowest surface energy. Therefore, our NWs with predominant {111} lateral facets appear as optimal candidates to be used as a model system in the study of doped-CeO_2 for applications in catalysis, gas sensors and oxygen ionic conductivity.

Acknowledgements

We acknowledge financial support from Spanish Ministry of Economy and Competitiveness through the "Severo Ochoa" Programme for Centres of Excellence in R&D (SEV-2013-0295 and SEV-2015-0496), CONSOLIDER Excellence Network (MAT2015-68994-REDC), COACHSUPENERGY project (MAT2014-51778-C2-1-R, co-financed by the European Regional Development Fund), and the projects MAT2011-28874-C02-01, ENE2014-56109-C3-3-R and Consolider Nanoselect (CSD2007-00041), and from the Catalan Government (2014-SGR-753, 2014-SGR-1638 and Xarmae). AQ and MdlM are also grateful for JAE-Predoc fellowship from CSIC (E-08-2012-1321248 and E-08-2013-1028356, co-financed by the European Social Fund). Authors also thank the INA-LMA facilities for the use of the advanced (S)TEM equipment.

Notes and references

1. S. R. Foltyn, L. Civale, J. L. MacManus-Driscoll, Q. X. Jia, B. Maiorov, H. Wang and M. Maley, *Nat. Mater.*, 2007, **6**, 631-642.
2. A. n. Carretero-Genevrier, J. Gázquez, J. C. Idrobo, J. Oró, J. Arbiol, M. a. Varela, E. Ferain, J. Rodríguez-Carvajal, T. Puig, N. s. Mestres and X. Obradors, *J. Am. Chem. Soc.*, 2011, **133**, 4053-4061.
3. S. J. Pearton, D. P. Norton and F. Ren, *Small*, 2007, **3**, 1144-1150.
4. C. Cen, S. Thiel, J. Mannhart and J. Levy, *Science*, 2009, **323**, 1026-1030.
5. W. Eerenstein, N. D. Mathur and J. F. Scott, *Nature*, 2006, **442**, 759-765.
6. Y. Wu, H. Yan and P. Yang, *Top. Catal.*, 2002, **19**, 197-202.
7. T. Ito and S. Okazaki, *Nature*, 2000, **406**, 1027-1031.
8. J. V. Barth, G. Costantini and K. Kern, *Nature*, 2005, **437**, 671-679.
9. A. S. Arico, P. Bruce, B. Scrosati, J.-M. Tarascon and W. van Schalkwijk, *Nat. Mater.*, 2005, **4**, 366-377.
10. M. Gibert, T. Puig, X. Obradors, A. Benedetti, F. Sandiumenge and R. Huhne, *Adv. Mater.*, 2007, **19**, 3937.
11. J. Zabaleta, M. Jaafar, P. Abellan, C. Monton, O. Iglesias-Freire, F. Sandiumenge, C. A. Ramos, R. D. Zysler, T. Puig, A. Asenjo, N. Mestres and X. Obradors, *J. Appl. Phys.*, 2012, **111**, 024307-024308.
12. A. Carretero-Genevrier, J. Gazquez, C. Magen, M. Varela, E. Ferain, T. Puig, N. Mestres and X. Obradors, *Chem. Comm.*, 2012, **48**, 6223-6225.
13. M. Gibert, T. Puig and X. Obradors, *Surf. Sci.*, 2007, **601**, 2680-2683.
14. X. Obradors, T. Puig, M. Gibert, A. Queralto, J. Zabaleta and N. Mestres, *Chem. Soc. Rev.*, 2014, **43**, 2200-2225.
15. A. Carretero-Genevrier, T. Puig, X. Obradors and N. Mestres, *Chem. Soc. Rev.*, 2014, **43**, 2042-2054.
16. Z.-A. Qiao, Z. Wu and S. Dai, *ChemSusChem*, 2013, **6**, 1821-1833.
17. Z. A. Feng, F. El Gabaly, X. Ye, Z.-X. Shen and W. C. Chueh, *Nat. Comm.*, 2014, **5**.
18. H. J. Beie and A. Gnörich, *Sens. Actuators B*, 1991, **4**, 393-399.
19. P. Jasinski, T. Suzuki and H. U. Anderson, *Sens. Actuators B*, 2003, **95**, 73-77.
20. N. Izu, W. Shin and N. Murayama, *Sens. Actuators B*, 2003, **93**, 449-453.
21. L. Almar, A. Tarancón, T. Andreu, M. Torrell, Y. Hu, G. Dezanneau and A. Morata, *Sens. Actuators B*, 2015, **216**, 41-48.
22. M. Kuhn, S. R. Bishop, J. L. M. Rupp and H. L. Tuller, *Acta Mater.*, 2013, **61**, 4277-4288.
23. E. P. Murray, T. Tsai and S. A. Barnett, *Nature*, 1999, **400**, 649-651.
24. W. C. Chueh, C. Falter, M. Abbott, D. Scipio, P. Furler, S. M. Haile and A. Steinfeld, *Science*, 2010, **330**, 1797-1801.
25. J. An, Y. B. Kim, J. Park, T. M. Gur and F. B. Prinz, *Nano Lett.*, 2013, **13**, 4551-4555.
26. Y. Shi, A. H. Bork, S. Schweiger and J. L. Rupp, *Nat. Mater.*, 2015, **14**, 721-727.
27. N. J. Divins, I. Angurell, C. Escudero, V. Pérez-Dieste and J. Llorca, *Science*, 2014, **346**, 620-623.
28. H.-F. Lu, Y. Zhou, W.-F. Han, H.-F. Huang and Y.-F. Chen, *Catal. Sci. Technol.*, 2013, **3**, 1480-1484.
29. C. G. Maciel, T. d. F. Silva, L. P. R. Profeti, E. M. Assaf and J. M. Assaf, *Appl. Catal. A*, 2012, **431–432**, 25-32.
30. M. A. Sainz, A. Durán and J. M. Fernández Navarro, *J. Non-Cryst. Solids*, 1990, **121**, 315-318.
31. M. G. Krishna, A. Hartridge and A. K. Bhattacharya, *Mater. Sci. Eng. B*, 1998, **55**, 14-20.
32. I. Porqueras, C. Person, C. Corbella, M. Vives, A. Pinyol and E. Bertran, *Solid State Ionics*, 2003, **165**, 131-137.

Please do not adjust margins

Please do not adjust margins

33. C. A. Copetti, H. Soltner, J. Schubert, W. Zander, O. Hollricher, C. Buchal, H. Schulz, N. Tellmann and N. Klein, *Appl. Phys. Lett.*, 1993, **63**, 1429-1431.
34. L. Tye, N. A. El-Masry, T. Chikyow, P. McLarty and S. M. Bedair, *Appl. Phys. Lett.*, 1994, **65**, 3081-3083.
35. A. Goyal, M. P. Paranthaman and U. Schoop, *MRS Bull.*, 2004, **29**, 552-561.
36. X. Obradors, T. Puig, A. Pomar, F. Sandiumenge, N. Mestres, M. Coll, A. Cavallaro, N. Roma, J. Gazquez, J. C. Gonzalez, O. Castano, J. Gutierrez, A. Palau, K. Zalamova, S. Morlens, A. Hassini, M. Gibert, S. Ricart, J. M. Moreto, S. Pinol, D. Isfort and J. Bock, *Supercond. Sci. Technol.*, 2006, **19**, S13-S26.
37. X. Obradors, T. Puig, S. Ricart, M. Coll, J. Gazquez, A. Palau and X. Granados, *Supercond. Sci. Technol.*, 2012, **25**, 123001.
38. R. W. Schwartz, T. Schneller and R. Waser, *C. R. Chim.*, 2004, **7**, 433-461.
39. A. Carretero-Genevrier, M. Gich, L. Picas, J. Gazquez, G. L. Drisko, C. Boissiere, D. Grosso, J. Rodriguez-Carvajal and C. Sanchez, *Science*, 2013, **340**, 827-831.
40. W. Lerch, *Phys. Status Solidi A*, 1996, **158**, 117-136.
41. R. A. Chapman, J. W. Kuehne, P. S. H. Ying, W. F. Richardson, A. R. Paterson, A. P. Lane, I. C. Chen, L. Velo, C. H. Blanton, M. M. Mosiehl and J. L. Paterson, Washington, DC, USA, 1991.
42. R. A. Chapman, M. Rodder, M. M. Moslehi, L. Velo, J. W. Kuehne and A. P. Lane, Taipei, Taiwan, 1993.
43. H. Suzuki, Y. Miwa, T. Naoe, H. Miyazaki, T. Ota, M. Fuji and M. Takahashi, *J. Eur. Ceram. Soc.*, 2006, **26**, 1953-1956.
44. S.-T. Chen, G.-S. Wang, Y.-Y. Zhang, L.-H. Yang and X.-L. Dong, *J. Am. Chem. Soc.*, 2007, **90**, 3635-3637.
45. E. M. Griswold, L. Weaver, M. Sayer and I. D. Calder, *J. Mater. Res.*, 1995, **10**, 3149-3159.
46. N. Keiichi and N. Shigetoshi, *Jpn. J. Appl. Phys.*, 1994, **33**, 5147.
47. Y. Cheng, H. Suo, L. Ma, Z. Zhang, Y. Xu and M. Liu, *CrystEngComm*, 2014, **16**, 8954-8959.
48. A. Queraltó, Universitat Autònoma de Barcelona, 2015.
49. A. Queraltó, M. De la Mata, J. Arbiol, X. Obradors and T. Puig, *Advanced Materials Interfaces*, 2016, DOI: 10.1002/admi.201600392, 1600392.
50. M. Gibert, P. Abellán, A. Benedetti, T. Puig, F. Sandiumenge, A. García and X. Obradors, *Small*, 2010, **6**, 2716-2724.
51. M. Gibert, P. Abellan, L. Martinez, E. Roman, A. Crespi, F. Sandiumenge, T. Puig and X. Obradors, *CrystEngComm*, 2011, **13**, 6719-6727.
52. N. Bassiri-Gharb, Y. Bastani and A. Bernal, *Chem. Soc. Rev.*, 2014, **43**, 2125-2140.
53. A. Regoutz, R. G. Egdell, D. Wermeille, R. A. Cowley and K. H. L. Zhang, *Nanoscale*, 2013, **5**, 7445-7451.
54. Y. Sun, Q. Liu, S. Gao, H. Cheng, F. Lei, Z. Sun, Y. Jiang, H. Su, S. Wei and Y. Xie, *Nat. Comm.*, 2013, **4**.
55. M. M. Branda, R. M. Ferullo, M. Causà and F. Illas, *J. Phys. Chem. C*, 2011, **115**, 3716-3721.
56. J. Zabaleta, N. Mestres, P. Abellan, M. Gibert, F. Sandiumenge, T. Puig and X. Obradors, *Nanotechnology*, 2010, **21**, 025302.
57. J. A. Rodriguez, J. Graciani, J. Evans, J. B. Park, F. Yang, D. Stacchiola, S. D. Senanayake, S. Ma, M. Pérez, P. Liu, J. F. Sanz and J. Hrbek, *Angew. Chem.*, 2009, **121**, 8191-8194.
58. M. Fronzi, S. Piccinin, B. Delley, E. Traversa and C. Stampfl, *Phys. Chem. Chem. Phys.*, 2009, **11**, 9188-9199.
59. C. Barth, C. Laffon, R. Olbrich, A. Ranguis, P. Parent and M. Reichling, *Sci. Rep.*, 2016, **6**, 21165.
60. J. Graciani, K. Mudiyanselage, F. Xu, A. E. Baber, J. Evans, S. D. Senanayake, D. J. Stacchiola, P. Liu, J. Hrbek, J. F. Sanz and J. A. Rodriguez, *Science*, 2014, **345**, 546-550.
61. S. D. Senanayake, D. Stacchiola, J. Evans, M. Estrella, L. Barrio, M. Pérez, J. Hrbek and J. A. Rodriguez, *J. Catal.*, 2010, **271**, 392-400.
62. P. Roura, J. Farjas, S. Ricart, M. Aklalouch, R. Guzman, J. Arbiol, T. Puig, A. Calleja, O. Peña-Rodríguez, M. Garriga and X. Obradors, *Thin Solid Films*, 2012, **520**, 1949-1953.
63. S. Bernal, F. J. Botana, J. J. Calvino, C. López-Cartes, J. A. Pérez-Omil and J. M. Rodríguez-Izquierdo, *Ultramicroscopy*, 1998, **72**, 135-164.
64. J. Arbiol, C. Magen, P. Becker, G. Jacopin, A. Chernikov, S. Schafer, F. Furtmayr, M. Tchernycheva, L. Rigutti, J. Teubert, S. Chatterjee, J. R. Morante and M. Eickhoff, *Nanoscale*, 2012, **4**, 7517-7524.
65. J. Arbiol, A. Cirera, F. Peiro, A. Cornet, J. R. Morante, J. J. Delgado and J. J. Calvino, *Appl. Phys. Lett.*, 2002, **80**, 329-331.
66. M. I. B. Utama, M. de la Mata, C. Magen, J. Arbiol and Q. Xiong, *Adv. Funct. Mater.*, 2013, **23**, 1636-1646.
67. M. Romeo, K. Bak, J. El Fallah, F. Le Normand and L. Hilaire, *Surf. Interface Anal.*, 1993, **20**, 508-512.
68. J. L. M. Rupp, B. Scherrer, N. Schäuble and L. J. Gauckler, *Adv. Funct. Mater.*, 2010, **20**, 2807-2814.
69. J. L. M. Rupp, B. Scherrer and L. J. Gauckler, *Phys. Chem. Chem. Phys.*, 2010, **12**, 11114-11124.
70. T. Schneller, R. Waser, M. Kosec and D. Payne, *Chemical Solution Deposition of Functional Oxide Thin Films*, Springer, London, 2013.
71. M. Coll, J. Gazquez, F. Sandiumenge, T. Puig, X. Obradors, J. P. Espinos and R. Huhne, *Nanotechnology*, 2008, **19**, 395601.
72. S. Turner, S. Lazar, B. Freitag, R. Egoavil, J. Verbeeck, S. Put, Y. Strauven and G. Van Tendeloo, *Nanoscale*, 2011, **3**, 3385-3390.
73. L. Wu, H. J. Wiesmann, A. R. Moodenbaugh, R. F. Klie, Y. Zhu, D. O. Welch and M. Suenaga, *Phys. Rev. B*, 2004, **69**, 125415.
74. S. Tsunekawa, T. Fukuda and A. Kasuya, *Surf. Sci.*, 2000, **457**, L437-L440.
75. S. Deshpande, S. Patil, S. V. N. T. Kuchibhatla and S. Seal, *Appl. Phys. Lett.*, 2005, **87**, 133113-133113.
76. P. Dutta, S. Pal, M. S. Seehra, Y. Shi, E. M. Eyring and R. D. Ernst, *Chem. Mater.*, 2006, **18**, 5144-5146.
77. K. Song, H. Schmid, V. Srot, E. Gilardi, G. Gregori, K. Du, J. Maier and P. A. van Aken, *APL Materials*, 2014, **2**, 032104.
78. M. López-Haro, J. M. Cíes, S. Trasobares, J. A. Pérez-Omil, J. J. Delgado, S. Bernal, P. Bayle-Guillemaud, O. Stéphan, K. Yoshida, E. D. Boyes, P. L. Gai and J. J. Calvino, *ACS Nano*, 2012, **6**, 6812-6820.
79. V. F. Solovyov, M. Gibert, T. Puig and X. Obradors, *Appl. Phys. Lett.*, 2010, **97**, 231904.

 This journal is © The Royal Society of Chemistry 20xx

Please do not adjust margins

Please do not adjust margins

80. J. Garcia-Barriocanal, A. Rivera-Calzada, M. Varela, Z. Sefrioui, E. Iborra, C. Leon, S. J. Pennycook and J. Santamaria, *Science*, 2008, **321**, 676-680.
81. M. Gibert, A. Garcia, T. Puig and X. Obradors, *Phys. Rev. B*, 2010, **82**, -.
82. V. A. Shchukin and D. Bimberg, *Rev. Mod. Phys.*, 1999, **71**, 1125-1171.
83. J. C. Nie, H. Yamasaki and Y. Mawatari, *Phys. Rev. B*, 2004, **70**, 195421.
84. J. Tersoff and R. M. Tromp, *Phys. Rev. Lett.*, 1993, **70**, 2782-2785.
85. M. Stengel, *Phys. Rev. B*, 2011, **84**, 205432.
86. J. C. Conesa, *Surf. Sci.*, 1995, **339**, 337-352.
87. J. A. Floro, M. B. Sinclair, E. Chason, L. B. Freund, R. D. Twesten, R. Q. Hwang and G. A. Lucadamo, *Phys. Rev. Lett.*, 2000, **84**, 701-704.
88. I. Szafraniak, C. Harnagea, R. Scholz, S. Bhattacharyya, D. Hesse and M. Alexe, *Appl. Phys. Lett.*, 2003, **83**, 2211-2213.

This journal is © The Royal Society of Chemistry 20xx

Please do not adjust margins